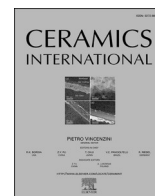




Contents lists available at ScienceDirect

Ceramics International

journal homepage: www.elsevier.com/locate/ceramint

The correlations between structural and optical properties of magnetite nanoparticles synthesised from natural iron sand

Heryanto Heryanto, Dahlang Tahir*

Department of Physics, Hasanuddin University, Makassar, 90245, Indonesia

ARTICLE INFO

Keywords:

Magnetite
XRD
Structural properties
FTIR
Optical properties
Optical phonon vibration

ABSTRACT

The correlations between structural and optical properties of magnetite (Fe_3O_4) nanoparticles were analyzed by using X-Ray Diffraction (XRD) and Fourier Transform Infrared (FTIR) Spectroscopy. The magnetite was synthesised from the iron sand using NaOH, HCl, and NaCl as a solvent. From the quantitative analysis of XRD spectra, the crystallite size (D), strain (ϵ), stress (σ), energy deformation (u), porosity, and specific surface area were determined. The Kramers Kronig (K–K) relations was applied to the FTIR spectra to determine the optical properties: refractive index (n), extinction coefficient (k), the complex dielectric function (ϵ), and the energy loss function ($\text{Im}(-1/\epsilon)$). The uniform strain was produced from the NaOH and HCl as the solvent. The magnetite had higher porosity with NaCl as a solvent and was directly proportional to the optical phonon vibration. We found a perfect correlation; when the difference between two optical phonon increases, the crystallite size decreases, and the strain will be uniform.

1. Introduction

Iron is one type of metal most widely used as a tool for supporting our daily life. Ionic type of iron include FeO, Fe_2O_3 , and Fe_3O_4 . Iron has different properties that are used for various applications. To date, considerable research has been devoted to studying Fe_3O_4 materials, such as synthesis via wet chemical reduction [1], corrosion in reinforced concrete structures [2], adsorption of alkaloids [3], and on the growth and oxidation of iron nanoparticles [4]. Several Fe_3O_4 potentials of also pH-responsive for imaging-guided tumour eradication by photo-thermal therapy [5], as a contrast agent for magnetic resonance imaging [6] or composite for absorber materials [7,8], and antimicrobials [9].

Some references reported the synthesis of Fe_3O_4 from iron sand using high energy milling [10], mechanical alloying [11], co-precipitation [12], sonochemical methods [13], and gamma irradiation [14]. The study of Fe_3O_4 using a vibrating sample magnetometer (VSM) reported in Ref. [12], phase characterisation, and magnetic properties that were prepared by wet mixing [13,15], and magnetite domain interactions [16]. The synthesis of magnetite using solvent HCl and NH_4OH reported in Ref. [17] which affect in decreasing crystallinity and particle size and for only HCl as a solvent reported in Refs. [18–20] and shows formation of magnetite single phase. The effects of divalent heavy metal cations to the magnetite phase in Ref. [21] and magnetite/silica nanocomposites

for drug delivery vehicle shows pure magnetite crystal phase synthesised using HCl [22,23]. The synthesised of magnetite nanoparticles using combination of solvents are: $\text{H}_2\text{SO}_4/\text{NaCl}$ [24], surfactant of tetramethylammonium hydroxide (TMAH) and NaCl [25], and two step synthesis by HCl and followed by NaCl [26]. However, the solvent used to synthesize magnetite from natural iron sand were reported using individual solvent only HCl and NH_4OH , and for combination of solvents such as: HCl followed by NaCl. Therefore, in this study, we used three type individual solvents are HCl, NaCl, and NaOH in synthesised methods. The effect of the various solvent in synthesised magnetite from iron sand to the structural and optical properties have not been investigated adequately. These properties are essential knowledge and the correlation between them also important to understand the performance of materials for various applications.

Hence, in this study, we synthesised the magnetite materials using NaOH, HCl, and NaCl as a solvent and characterised by XRD and FTIR. We applied the Scherrer, Williamson-Hall (W–H), and size strain plot (SSP) methods to study the structural properties using a quantitative analysis of X-Ray Diffraction (XRD) spectra. These analyses are resulted in important information, including crystallite size (D), strain (ϵ), stress (σ), and energy deformation (u). The Kramers-Kronig (K–K) relations were used to determine the optical properties from a quantitative analysis of Fourier Transform Infrared Spectroscopy (FTIR) spectra.

* Corresponding author.

E-mail address: dtahir@fmipa.unhas.ac.id (D. Tahir).

<https://doi.org/10.1016/j.ceramint.2021.02.255>

Received 21 December 2020; Received in revised form 2 February 2021; Accepted 27 February 2021

Available online 3 March 2021

0272-8842/© 2021 Elsevier Ltd and Techna Group S.r.l. All rights reserved.

Using the refractive index (n) and extinction coefficient (k), we analyzed the optical phonon vibrations, determine the complex dielectric function ($\epsilon = \epsilon' + i\epsilon''$) and energy loss function ($\text{Im}(-1/\epsilon(\omega)) = (\epsilon_1(\omega))/((\epsilon_1^2(\omega) + \epsilon_2^2(\omega)))$).

2. Material and experimental details

The iron sand sample is from Pantai Lere, Bima Regency, Nusa Tenggara Barat Province, Indonesia (-8.866147° , 118.527858°). We used three kinds of solution: sodium hydroxide (NaOH) produced by Merck, hydrogen chloride (HCl) produced by Merck, and salt powder produced by the local industry "Refina Garam Meja" Indonesia. The amounts of each solution by slowly dropping 3 g of iron sand were as follows:

sample 1 = 3 g NaOH solution (0.1 M) + 3 g iron sand

sample 2 = 3 g HCl solution (0.1 M) + 3 g iron sand, and

sample 3 = (3 g Salt powder + 3g H_2O) + 3 g iron sand

The samples were maintained at room temperature for 12 h. The final samples were heated in a free oxygen environment at 80°C for 6 h and then stirred at 10 Hz for 10 min. All samples were cleaned with water to remove the solution's contamination and controlled using X-ray fluorescence (X-RF). The dried samples were stored in a desiccator for further use.

The structural properties of the pure iron sand and extracted Fe_3O_4 powder were analyzed using X-ray diffraction via Shimadzu 7000 CuK α radiation in step of 0.02° per min and angles from are 25° to 75° . The optical properties were determined from the quantitative analysis of the transmission Fourier transform infrared (FTIR) spectra (Shimadzu Corp) at the wavenumber 400 to 900 cm^{-1} . To prepare our samples for FTIR characterisation, we used KBr because it has a wide spectral range. It produced smooth, thin, and transparent discs when mixed with the powdered samples [27]. Approximately 0.5 g of each sample are mixed with 50 g KBr and then pressed into 1 mm disc in a hydraulic press at 10.000 psi for 3 min to form pellets.

3. Result and discussion

3.1. X-ray diffraction analysis

The XRD patterns of the magnetite in this study were extracted by various solvents and are shown in Fig. 1. The diffraction peak intensity showed that the impurity concentration of the iron sand's diffraction peaks at 33.5° and 56° decreased due to the solvent's effect. The XRD spectra also detected magnetite phase structures. The next analysis used these spectra to determine the structural properties using the Scherrer, Williamson-Hall (WH), and size strain plot (SSP) models.

The XRD spectra confirmed that the magnetite's diffraction peaks had cubic structures, and the peak broadening may have been due to the type of solution: acid, base, or salt solution. Peak broadening at 35° - 37° in the different solutions as shown in Fig. 2 clearly demonstrates the different intensity (a) and (b) relation between the crystal lattice and strain [28]. Fig. 2(a) clearly shows two kinds of strain: uniform and non-uniform strain.

The solvents' effect on the strain was as follows: the Fe_3O_4 with NaOH, HCl, and NaCl as solvents had uniform strain that shifted to a higher 2θ and lower 2θ , and small non-uniform strain shifted to a lower 2θ , respectively, from the iron sand's diffraction peaks at 35.96° with a (311) crystal orientation due to the differences in the distances between the atomic layers (d). The larger d spacing scale shifted lower and vice versa. The calculated lattice parameters and porosity shown in Table 1 were obtained using the following equations [29]:

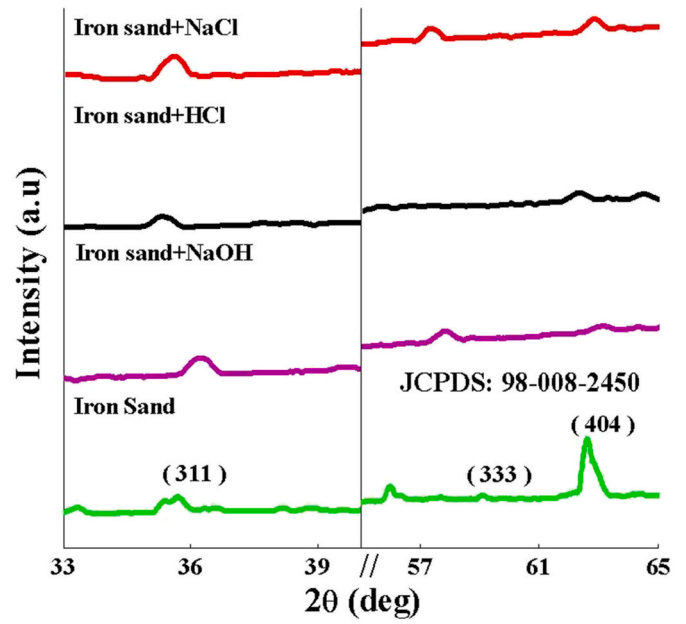


Fig. 1. The crystal orientation of Fe_3O_4 compared with JCPDS: 98-008-2450.

$$d = \frac{a}{\sqrt{h^2 + k^2 + l^2}} \quad (1)$$

$$V = a^3 \quad (2)$$

Lattice parameter is a for two-dimensional distance between the atomic layers or d -spacing (d), hkl are the Miller indices of the crystal orientations, and V is the cubic structure unit cell volume.

In this experiment, the samples' mass (m), X-ray density (ρ_x), experimental density (ρ_{ex}), and porosity (P) were determined using the following equation:

$$P = \left(1 - \frac{\rho_{ex}}{\rho_s}\right) \times 100\% \quad (3)$$

Details regarding the calculation porosity were previously reported in Ref. [30].

Microstructure can be calculated using [31]:

$$\rho_{ex} t_{\text{Fe}_3\text{O}_4} = \frac{2}{S_{A, \text{face}}} \quad (4)$$

Where ($t_{\text{Fe}_3\text{O}_4}$) is the layer thickness, and ($S_{A, \text{face}}$) is the surface area, which was determined using the following equation:

$$S_{A, \text{face}} = 2A_{UC} \frac{N_A}{M_w} \quad (5)$$

For the effect peak broadening, the two dimensional distance layer and inter-layer distance ($t_{\text{int, layer}}$) using the following equation:

$$t_{\text{int, layer}} = d_{\text{max}} - t_{\text{Fe}_3\text{O}_4} = \frac{1}{\left(\rho_{\text{dry}} \frac{S_{A, \text{faces}}}{2}\right) - t_{\text{Fe}_3\text{O}_4}} \quad (6)$$

Table 2 shows the thickness of single-layer Fe_3O_4 ($t_{\text{Fe}_3\text{O}_4}$), thickness of the interlayer ($t_{\text{int, layer}}$), surface area ($S_{A, \text{face}}$), density (ρ), and area total (Area, \AA^2). The specific surface area of the Fe_3O_4 extracted using NaCl as a solvent had the lowest value compared to other solvents. However, it showed that higher porosity may have occur due to the solvents' corrosive effects.

X-ray diffraction peak broadening was used to determine the crystallite size (D) and lattice strain (ϵ). The Scherrer equation was used to calculate the crystallite size from the full width at half maximum (β) and

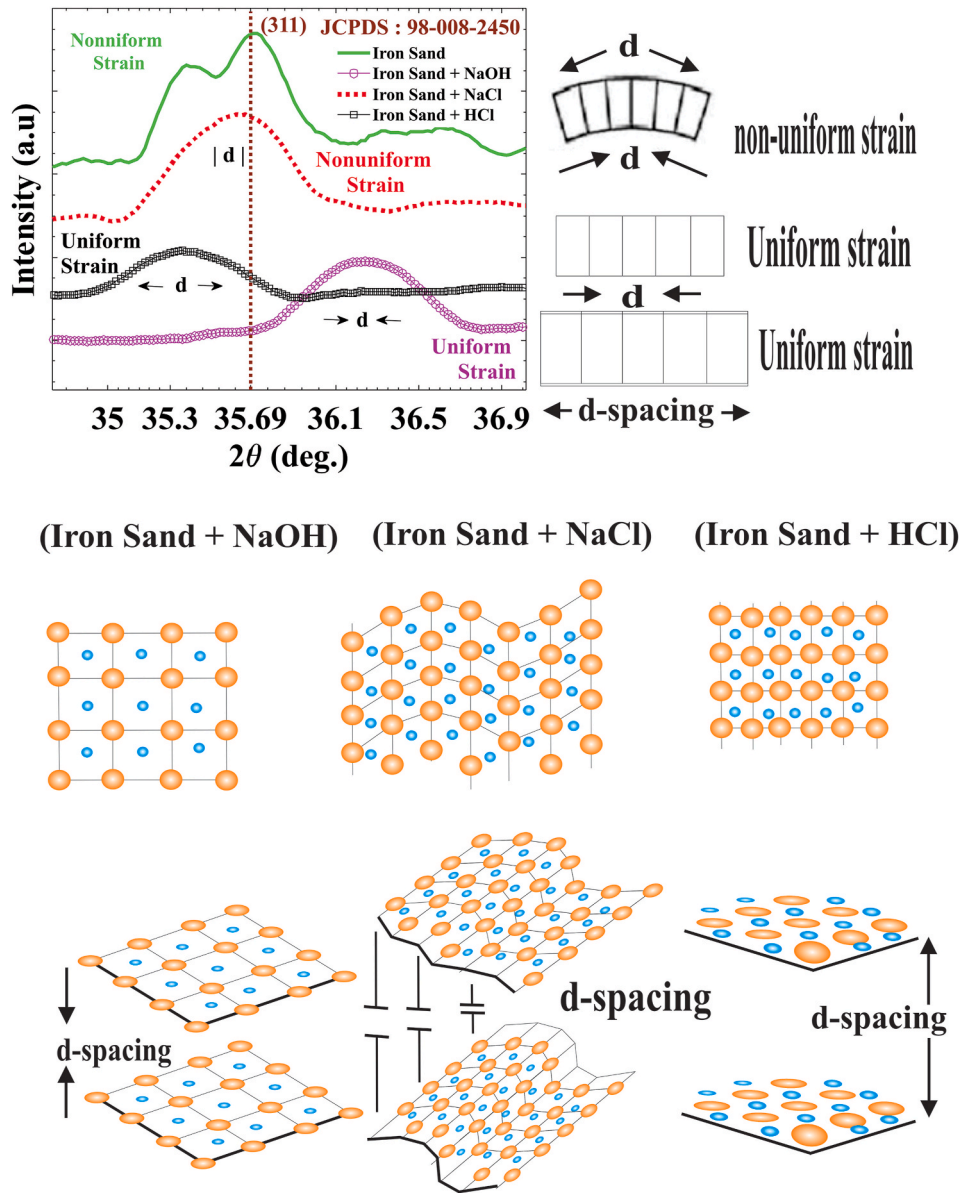


Fig. 2. X-ray diffraction angle positions of iron sand and several solvents (first rows (left)), we have included illustration by the effect of no strain, uniform strain and non-uniform strain on the peak broadening from x-ray spectra [16] (first rows (right)). The illustration of the lattice structure (second rows) and d-spacing (d) (third rows) for various solvent: NaOH (left), NaCl (middle), and HCl (right).

Table 1

Lattice parameter a (Å), volume (V), and porosity (%) from the quantitative analysis of XRD spectra in Fig. 1.

Sample	lattice parameter (Å)		range of error		Volume (Å ³)			Porosity-	Porosity-	Porosity-
	a	error a	a-min	a-max	V-min	V-max	V-med	max (%)	min (%)	med (%)
Iron Sand	8.37	0.0010	8.3690	8.3710	586.1661	586.5864	586.3763	94.3342	94.3382	94.3362
Iron Sand + NaOH	8.35	0.0008	8.3492	8.3508	582.0056	582.3602	582.1829	94.3750	94.3784	94.3767
Iron Sand + HCl	8.31	0.0012	8.3088	8.3112	573.6076	574.1048	573.8562	94.4547	94.4595	94.4571
Iron Sand + NaCl	8.22	0.00132	8.2187	8.2213	555.1447	555.6799	555.4123	94.6327	94.6379	94.6353

peak position (θ). These relationships were demonstrated in detail in our previously published reports [29,32, and 33]. The corresponding results are shown in Table 3.

$$\beta^2 = \beta_{measures}^2 - \beta_{instrumental}^2 \quad (7)$$

$$D = \frac{k\lambda}{\beta \cos \theta} \quad (8)$$

As reported in Ref. [34], the peak broadening was caused by the accumulated of the crystallite size and lattice strain.

Fig. 3 shows the Williamson-Hall (WH), uniform deformation (UDM), uniform stress deformation (USDm), uniform deformation energy density (UEDm), and size strain plot methods (SSP) for the corresponding results shown in Table 3. Details on these calculations are in Refs. [29,32,35and36]. The W-H and SSP plot analysis is shown in Table 3.

Table 2

Specific surface area $S_{A,face}$ ($\text{\AA}^2/\text{g}$), thickness of a single layer $t_{Fe_3O_4}$ (\AA), and the interlayer distance $t_{int.layer}$ (\AA).

Sample code	d spacing \AA	Area (\AA^2)	$\rho_{Fe_3O_4}$ g/cm^3	$S_{A,face}$ $(\text{\AA}^2/\text{g})$	$t_{Fe_3O_4}$ \AA	$t_{int.layer}$ \AA
Iron Sand	2.515	70.0569	4.08	3.64E+23	1.345	1.171
Iron Sand + NaOH	2.479	69.7225	4.08	3.63E+23	1.351	1.128
Iron Sand + HCl	2.537	69.0568	4.08	3.59E+23	1.364	1.173
Iron Sand + NaCl	2.521	67.5684	4.08	3.51E+23	1.394	1.126

Table 3

Slope (a) and y-intercept (b) determined from Fig. 3.

code	Y = ax+b	UDM	USDM	UEDDM	SSP
Iron Sand	a	-0.0015	-0.000524	-6.27E-04	0.0101
	b	0.007427	0.007427	0.007427	-2.612E-06
Iron Sand + NaOH	a	-0.001138	-0.0004	-0.00048	0.0217
	b	0.011541	0.011542	0.011542	-7.0754E-06
Iron Sand + HCl	a	-0.001021	-0.00036	-0.00043	0.0146
	b	0.009762	0.009763	0.009763	-3.259E-06
Iron Sand + NaCl	a	0.001510	0.000529	0.000632	0.0193
	b	0.007516	0.007516	0.007516	-5.8744E-06

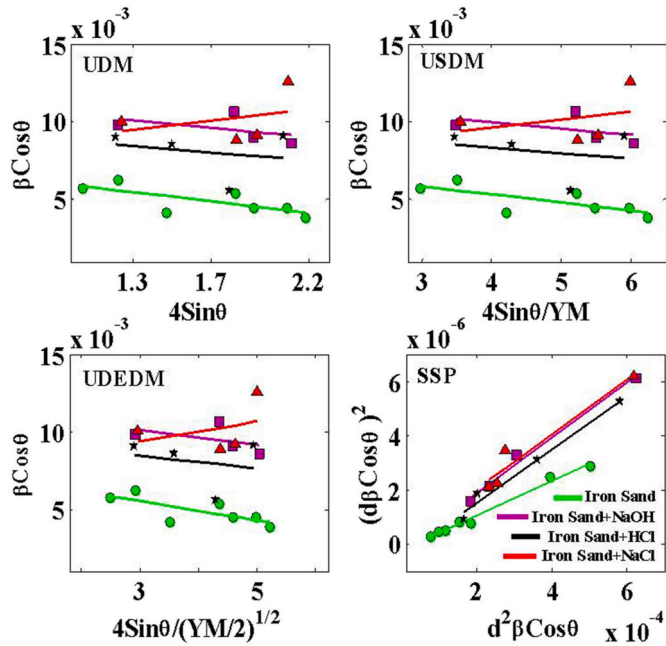


Fig. 3. Williamson-Hall analysis and Size Strain plot method. Diffraction peaks indicated by symbol, and linear fit analysis indicated by solid line.

Fig. 3 shows the slope and y intercept of the fitted lines (strain for UDM analysis, stress for USDM analysis, and Energy density for UEDDM analysis) and crystallite size. Table 3 shows the negative and positive linear fitting values due to the lattice shrinkage and lattice rearrangement, respectively, as reported in Ref. [37].

The linear fitting results are summarised in Table 3. The negative and positive y intercept values indicated that the solvents affected the structural properties of the acid and base solutions. The negative lattice value of the Fe_3O_4 was caused by shrinkage, and the salt was estranged [38]. The crystallite size, micro-strain, stress, and energy density are

presented in Table 4.

Fig. 2 the diffraction peak of the crystal plane (311) for various solvent and the relation between crystal lattice with d-spacing (d). The diffraction peaks for iron sand shows 2 peaks, the satellite peaks probably come from the impurity of the iron sand which lower 0.18° than the main peaks. For the iron sand after soaking with NaOH as a solvent shows crystal lattice is uniform strain shift to the higher 2θ indicated that some of the Fe atoms is properly sitting in the lattice structure but still unstable position [39]. For NaCl as solvent shows small shift to the lower 2θ indicated that Fe atoms are still adjusting to find good position in the lattice structure but for HCl as a solvent shows uniform strain with diffraction peak shifts to the lower 2θ is due to the Fe atoms fill the stable position in the lattice structure [39]. The illustration of lattice structure as shown in Fig. 2 (second rows) and d spacing (d) in Fig. 2 (third rows) for various solvent: NaOH (left), NaCl (middle), and HCl (right). The effect of HCl as a solvent to the structural properties of magnetite from iron sand analyzed by the XRD spectrum are: reduction crystallinity and particle size [17], single phase with lattice parameter 8.393 \AA [18], cluster microstructures of the primary particles associated with magnetic properties [40], and pure magnetite crystal phase [22].

The quantitative analysis of the XRD spectra presented in Fig. 2 shows that the structural properties and crystallite size decreased in all of the solvents, probably due to the structural modification of the iron sand that removed some impurities, shifting and broadening the main peaks [41,42]. Comparing each calculation model of the quantitative analysis of the XRD spectra showed good agreement for the crystallite size. The Scherrer method was higher than the other methods due to the number of parameters affected by the calculations. The Scherrer method calculated only the FWHM, 2θ diffraction, Young's modulus, and distances between the atoms.

3.2. FTIR analysis

Refractive index (n) and extinction coefficient (k) as a function of the wavenumber (ω) from the quantitative analysis of the Fourier transform infrared spectra were determined using the Kramers-Kronig (K-K) relations. In this study, a 1 mm disc of KBr was mixed with the powder samples to characterise the FTIR transmission spectroscopy. When mixed with powder samples, KBr will produce smooth, thin, and transparent discs [27]. Fig. 4 shows the FTIR spectra of the natural iron sand and Fe_3O_4 with the various solvents. The absorption peak at 560 cm^{-1} was the vibration of the Fe-O bond [27,43].

Fig. 4 shows the percent transmittance (T%) between the light intensity transmitted through the samples (I) to the incident light intensity (I_0). These spectra were converted to the reflection ($R(\omega)$) using the following well-known expressions [28,31,44,45]:

$$A(\omega) = 2 - \log[T(\omega)\%] \quad (9)$$

$$R(\omega) = 100 - [T(\omega) + A(\omega)] \quad (10)$$

To ascertain the refractive index (n) and extinction coefficient (k), first the phase change $\phi(\omega)$ was determined by:

$$\phi(\omega) = -\frac{\omega}{\pi} \int_0^{\infty} \frac{\ln R(\omega') - \ln R(\omega)}{\omega'^2 - \omega^2} \quad (11)$$

To solve equation (11), we applied the K-K relation and equation (12) for simple computations:

$$\phi(\omega_j) = -\frac{4\omega_j}{\pi} \Delta\omega \sum_i \frac{\ln(\sqrt{R(\omega)})}{\omega_i^2 - \omega_j^2} \quad (12)$$

Where, j is a series of wavenumber. If j is an odd number, i is 2,4,6,8, ..., j-1, and j+1, and when j is an even number, i is 1,3,5,7, ..., j-1, j+1, ... $\Delta\omega = \omega_{i+1} - \omega_i$. equation (12) was the input parameter for determining the refractive index (n) and extinction coefficient (k) using the following

Table 4

Size (nm), Strain ($\times 10^{-3}$), Stress (MPa) and Density of energy (kJ/m^3) determined from quantitative analysis of XRD spectra in Fig. 1.

data	Scherrer		Williamson-Hall Method						U	Size - Strain					
	Equation		UDM		USDm		UDEDm			Plot Method					
	D	ϵ	D	E	D	E	σ	D		E	σ	D	ϵ	σ	U
	nm	10^{-3}	nm	10^{-3}	nm	10^{-3}	Mpa	nm		10^{-3}	Mpa	kJ/m^{-3}	nm	10^{-3}	Mpa
Iron Sand	26.21	0.0055										24.9	0.93	288	134
	24.20	0.0051													
	36.38	0.0028													
	27.97	0.003	20.34	1.498	20.35	1.4971	524	20.3	1.5	370	393				
	33.64	0.0023													
	33.62	0.0022													
Iron Sand + NaOH	39.33	0.0018													
	15.02	0.0081	20.1	1.51	20.1	1.511	529	20.1	1.51	529	399.4	25	1.532	475	364.21
	16.98	0.0049													
Iron Sand + HCl	16.45	0.0048													
	11.96	0.006													
	16.71	0.0074	15.48	1.021	15.48	1.0288	360	15.5	1.03	360	184.9	17	1.141	353	202.06
Iron Sand + NaCl	17.63	0.0057													
	26.92	0.0031													
	16.59	0.0044													
	15.37	0.008	13.09	1.138	13.09	1.143	400	13.1	1.15	401	230.4	11.6	1.682	521	438.67
	14.16	0.0059													
	16.73	0.0047													
	17.58	0.0041													

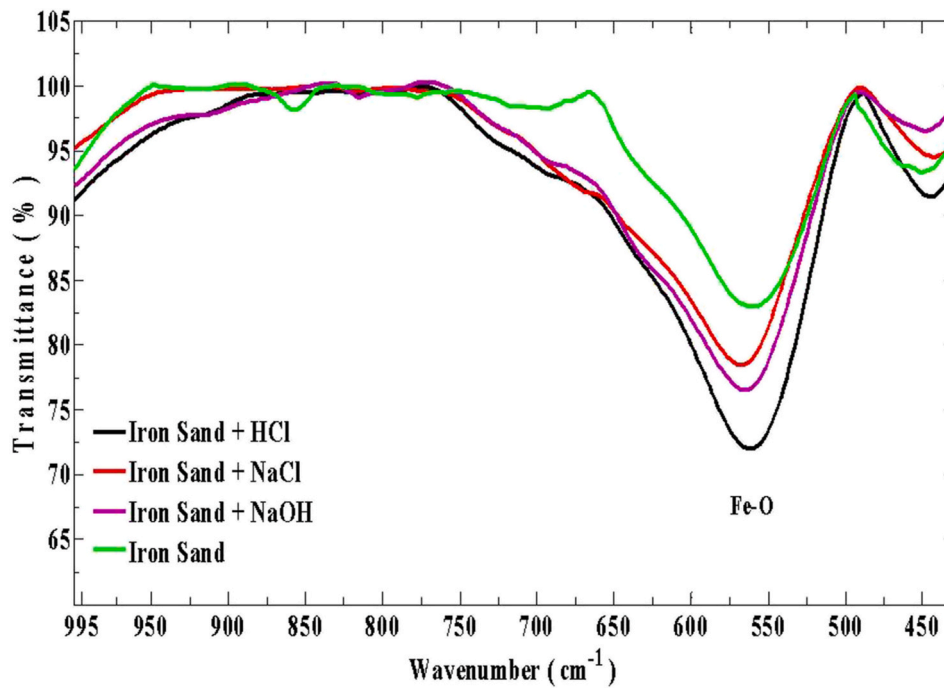


Fig. 4. FTIR spectra by the irons sand and Fe_3O_4 for various solvent.

equations:

$$n(\omega) = \frac{1 - R(\omega)}{1 + R(\omega) - 2\sqrt{R(\omega)}\cos\phi(\omega)} \quad (13)$$

$$k(\omega) = \frac{2\sqrt{R(\omega)}\sin\phi(\omega)}{1 + R(\omega) - 2\sqrt{R(\omega)}\cos\phi(\omega)} \quad (14)$$

The calculation results using equation (13) and (14) are shown in the first rows in Fig. 5.

The real part of refractive index indicated by n and the imaginary part or extinction coefficient indicated by k are shown in the first rows in Fig. 5. The transverse optical (TO) and longitudinal optical phonons (LO) were identified by the intersections between $n(\omega)$ and $k(\omega)$

indicated by TO and LO as shown in the first rows in Fig. 5. The dielectric function was also determined by the equation: $\tilde{\epsilon}(\omega) = \epsilon_1(\omega) + i\epsilon_2(\omega)$, where $\epsilon_1(\omega)$ is the real part and $\epsilon_2(\omega)$ is the imaginary part determined from the relation with n and k as follows:

$$\epsilon_1(\omega) = n^2(\omega) - k^2(\omega) \quad (15)$$

$$\epsilon_2(\omega) = 2n(\omega)k(\omega) \quad (16)$$

The calculation results of the ϵ_1 and ϵ_2 spectra based on equations (14) and (15), respectively, are shown in the second rows in Fig. 5.

The maximum ϵ_1 peaks shifted to lower wavenumbers and ϵ_2 shifted to higher wavenumbers due to the effects the acid solutions and crystal fields, which affected the structural and electrical properties of the

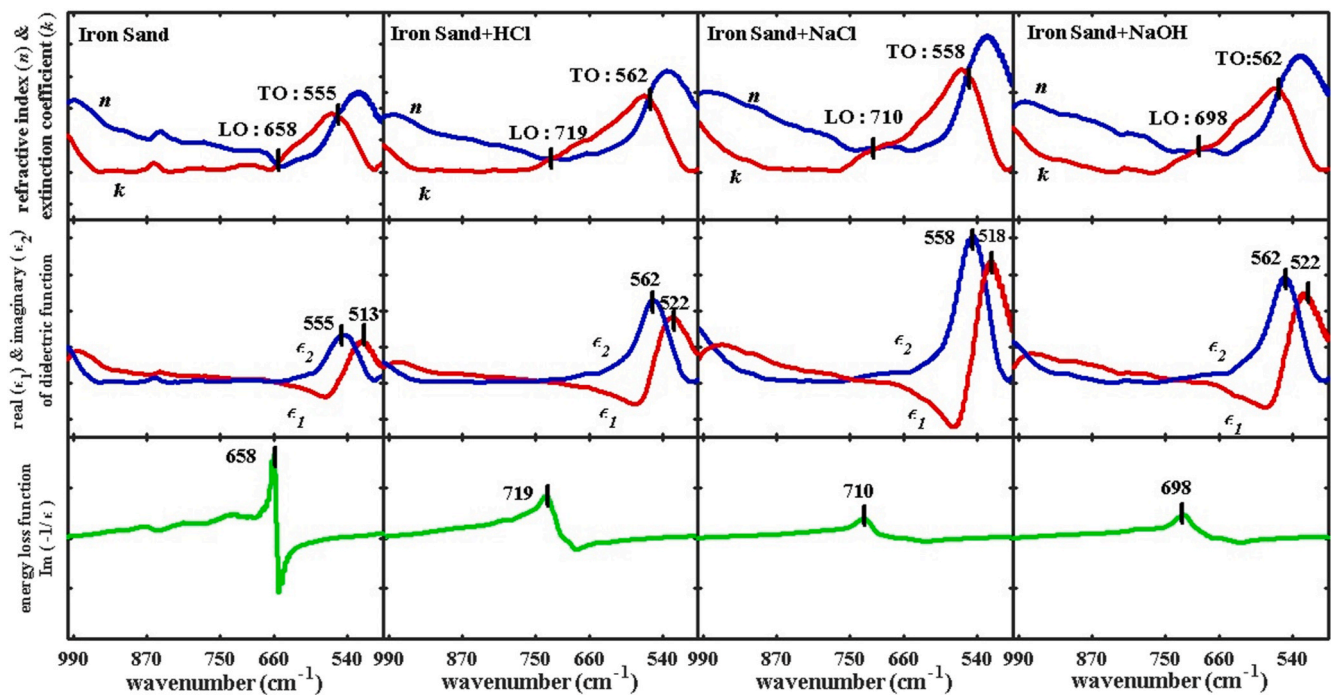


Fig. 5. The complex refractive index $\hat{n}(\omega) = n(\omega) + k(\omega)$ real part and imaginary part (first row), dielectric function ($\bar{\epsilon}(\omega) = \epsilon_1(\omega) + i\epsilon_2(\omega)$) (second row), and energy loss function ($\text{Im}(-1/\epsilon(\omega)) = \epsilon_2(\omega)/(\epsilon_1^2(\omega) + \epsilon_2^2(\omega))$) (third row) for natural iron sand powder and Fe_3O_4 for various solvents.

Fe_3O_4 [46–48]. There were two ways to identify the TO and LO modes; first, from the intersections between $n(\omega)$ and $k(\omega)$ as described in the first row in Fig. 5. The second was from the prominent peak position of the imaginary part ($\epsilon_2(\omega)$) of the dielectric function as shown in the second rows in Fig. 5 for the TO mode and energy loss function ($\text{Im}(-1/\epsilon(\omega)) = \epsilon_2(\omega)/(\epsilon_1^2(\omega) + \epsilon_2^2(\omega))$) and in the third rows in Fig. 5 for the LO mode [28,29]. Ref. [31,49–55] reported a quantitative analysis of electron spectroscopy spectra to determine the energy loss function ($\text{Im}(-1/\epsilon(\omega))$) and showed that the prominent peak position was considered the plasma frequency. Using our previous reports on composite cement/ $\text{BaSO}_4/\text{Fe}_3\text{O}_4$ and from the quantitative analysis of the FTIR spectra in Ref. [55], we also clearly demonstrated that the prominent peak position of ($\text{Im}(-1/\epsilon(\omega))$) was the plasma frequency.

The optical properties change for different solvent may due to the cohesion force between the iron sand atoms and some of the solvent atoms bonding together but still rearranged to form stable bonding with a new structure [7,31and39]. The stable bonding formation indicated by the distance between two optical phonon modes ($\Delta(\text{LO-TO})$) is higher which consistent by the analysis of XRD spectra for uniform strain with diffraction peak shifts to the lower 2θ . For lower distance between two optical phonon modes ($\Delta(\text{LO-TO})$) indicated that the non-uniformity cross-linking and less stable crystal structure [56–59].

Fig. 6 shows the relationship between the porosity, crystallite size, and different of the optical phonons ($\Delta(\text{LO-TO})$).

Fig. 6 clearly shows that the ($\Delta(\text{LO-TO})$) of the optical phonons increased when the crystallite size decreased, which was probably due to the structural properties transforming into uniform strain, leading to reduced vibrations [60]. The porosity was directly proportional to the optical properties ($\Delta(\text{LO-TO})$), similar to the results reported in Ref. [61].

4. Conclusions

Fe_3O_4 was successfully synthesised using various solvents: acid, base, and salt solutions. The XRD patterns showed that the crystallite size of the magnetite extracted using salt as a solvent was smaller than the other solvents. The optical properties were determined from the quantitative

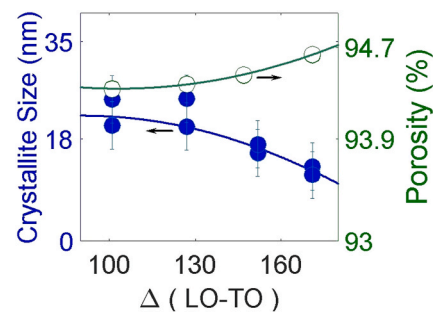


Fig. 6. Crystallite size value indicated by blue symbol, porosity value indicated by green open symbol, and linear fitting evaluated by solid line. (For interpretation of the references to color in this figure legend, the reader is referred to the Web version of this article.)

analysis of the FTIR spectra by applying the K-K relations. The magnetite's higher porosity with NaCl as a solvent was directly proportional to the optical phonon vibrations. We found very good correlations when the LO-TO of optical phonons increased, the crystallite size decreased, and the strain was uniform.

Declaration of competing interest

The authors declare that they have no known competing financial interests or personal relationships that could have appeared to influence the work reported in this paper.

Acknowledgments

This work was supported by the PD (Penelitian Dasar) 2020 funded by the Indonesian Government (DIKTI).

References

- [1] S.H. Chaki, T.J. Malek, M.D. Chaudhary, J.P. Taylor, M.P. Deshpande, Magnetite Fe_3O_4 nanoparticles synthesis by wet chemical reduction and their characterization, *Adv. Nat. Sci. Nanosci. Nanotechnol.* 6 (2015), 035009, <https://doi.org/10.1088/2043-6262/6/3/035009>.
- [2] A. Ouglova, Y. Berthaud, M. Francois, F. Focht, Mechanical properties of an iron oxide formed by corrosion in reinforced concrete structure, *Corrosion Sci.* 48 (2006) 3988–4000, <https://doi.org/10.1016/j.corsci.2006.03.007>.
- [3] L. Yang, J. Tian, J. Meng, R. Zhao, C. Li, J. Ma, T. Jin, Modification and characterization of Fe_3O_4 nanoparticles for use in adsorption of alkaloids, *Molecules* 23 (2018) 562, <https://doi.org/10.3390/molecules23030562>.
- [4] B. Wang, Q. Wie, S. Qu, Synthesis and characterization of uniform and crystalline magnetite nanoparticles via oxidation-precipitation and modified co-precipitation Methods, *Int. J. Electrochem. Sci.* 8 (2013) 3786–3793, <https://www.electrochemsci.org/papers/vol8/80303786.pdf>.
- [5] L.J.- Hua, W. Lei, Z.T.- Qi, W.J. Qiu, G. Xue, C.F. Zhi, Z.J.- Jun, L. Bo, S. Zhan, Facile synthesis of biocompatible Fe_3O_4 -based nanoparticles for pH-responsive dual-modal magnetic resonance imaging-guided tumor eradication by photo thermal therapy, *Chin. J. Anal. Chem.* 47 (5) (2019) 678–685, [https://doi.org/10.1016/S1872-2040\(19\)61158-8](https://doi.org/10.1016/S1872-2040(19)61158-8).
- [6] H. Basti, L.B. Tahar, L.S. Smiri, F. Herbst, M.-J. Vaulay, F. Chau, S. Ammar, S. Bendoric, Catechol derivatives-coated Fe_3O_4 and $\gamma\text{-Fe}_2\text{O}_3$ nanoparticles as potential MRI contrast agents, *J. Colloid Interface Sci.* 341 (2010) 248–254, <https://doi.org/10.1016/j.jcis.2009.09.043>.
- [7] D. Tahir, S. Ilyas, B. Abdullah, B. Armynah, H.J. Kang, Electronic properties of composite iron (II, III) oxide (Fe_3O_4) carbonaceous absorber materials by electron spectroscopy, *J. Electron. Spectrosc. Relat. Phenom.* 229 (2018) 47–51, <https://doi.org/10.1016/j.elspec.2018.09.008>.
- [8] S. Ilyas, B. Abdullah, D. Tahir, Enhancement of absorbing frequency and photocatalytic performance by temperature treatment of composites Fe_3O_4 -AC nanoparticle, *Adv. Powder Technol.* 31 (3) (2020) 905–913, <https://doi.org/10.1016/j.apt.2019.11.007>.
- [9] P. Kulkarni, G.A. Raspanti, A.Q. Bui, R.N. Bradshaw, K.E. Kniel, P.C. Chiu, M. Sharma, A. Sapkota, A.R. Sapkota, Zerovalent iron-sand filtration can reduce the concentration of multiple antimicrobials in conventionally treated reclaimed water, *Environ. Res.* 172 (2019) 301–309, <https://doi.org/10.1016/j.envres.2019.02.012>.
- [10] Y.E. Gunanto, M.P. Izaak, E. Jobiling, L. Cahyadi, W.A. Adi, High purity Fe_3O_4 from local iron sand extraction, *J. Phys. Conf.* 1011 (2018), 012005, <https://doi.org/10.1088/1742-6596/1011/1/012005>.
- [11] Z. Jalil, A. Rahwanto, Akhyar Mustanir, E. Handoko, Magnetic behavior of natural magnetite (Fe_3O_4) extracted from beach sand obtained by mechanical alloying method, *AIP Conference Proceedings* 1862 (2017), 030023, <https://doi.org/10.1063/1.4991127>.
- [12] R. Rahmawati, A. Taufiq, S. Sunaryono, A. Fuad, B. Yulianto, S. Suyatman, D. Kurniadi, Synthesis of magnetite (Fe_3O_4) Nanoparticles from iron sands by co precipitation-ultrasonic methods, *J. Mater. Environ. Sci.* 9 (1) (2018) 155–160, <https://doi.org/10.26872/jmes.2018.9.1.19>.
- [13] R. Rahmawati, Y.V. Kaneti, A. Taufiq, A.S. Sunaryono, B. Yulianto, S. Suyatman, N. Nugraha, D. Kurniadi, Md S. Hossain, Y. Yamauchi, Green synthesis of magnetite nanostructures from naturally available iron sands via sonochemical method, *Bull. Chem. Soc. Jpn.* 91 (2) (2018) 311–317, <https://doi.org/10.1246/bcsj.20170317>, 2018.
- [14] D. Ghanbari, M.S. Niasari, M.G. Kooch, A sonochemical method for synthesis of Fe_3O_4 nanoparticles and thermal stable PVA-based magnetic nanocomposite, *J. Ind. Eng. Chem.* 20 (2014) 3970–3974, <https://doi.org/10.1016/j.jiec.2013.12.098>.
- [15] A. Abedini, A.R. Daud, M.A.A. Hamid, N.K. Othman, Methods and strategies for the synthesis of diverse nanoparticles and their applications: a comprehensive overview, *J. PLoS ONE* 9 (2014) 1–8, <https://doi.org/10.1039/C5RA19388E>.
- [16] N. Munasir, S. Setyaningsih, Z.A. Yanasin, A. Supardi, Sunaryono Taufiq, Phase and magnetic properties of $\text{Fe}_3\text{O}_4/\text{SiO}_2$ natural materials based using polyethylene glycol media, *IOP Conf. Ser. Mater. Sci. Eng.* 515 (2019), 012017, <https://doi.org/10.1088/1757-899X/515/1/012017>.
- [17] Fathurrahmi Rahmi, F.P. Wati, Preparation of magnetic chitosan using local iron sand for mercury removal, *Heliyon* 5 (2019), e01731, <https://doi.org/10.1016/j.heliyon.2019.e01731>.
- [18] P. Simamora, C.S. Saragih, D.P. Hasibuan, J. Rajagukguk, Synthesis of nanoparticles Fe_3O_4 /PEG/PPy-based on natural iron sand, *Materials Today Proceedings* 5 (7) (2018) 14970–14974, <https://doi.org/10.1016/j.matpr.2018.04.040>, Part 1.
- [19] A. Taufiq, F.N. Ikasari, D. Yuliantika, S. Sunaryono, N. Mufti, H. Susanto, E. Suarsini, N. Hidayat, A. Fuad, A. Hidayat, M. Diantoro, Structural, magnetic, optical and antibacterial properties of magnetite ferrofluids with PEG-20000 template, *Materials Today Proceedings* 17 (Part 4) (2019) 1728–1735, <https://doi.org/10.1016/j.matpr.2019.06.204>.
- [20] M. Rianna, M. Situmorang, C. Kurniawan, A.P. Tetuko, E.A. Setiadi, M. Ginting, P. Sebayang, The effect of Mg-Al additive composition on microstructure, magnetic properties, and microwave absorption on $\text{BaFe}_{12-2x}\text{Mg}_x\text{Al}_x\text{O}_{19}$ ($x = 0-0.5$) material synthesized from natural iron sand, *Mater. Lett.* 256 (2019) 126612, <https://doi.org/10.1016/j.matlet.2019.126612>.
- [21] H. Huang, J. Wang, R. Yao, B.C. Bostick, H. Prommer, X. Liu, J. Sun, Effect of divalent heavy metal, cations on the synthesis and characteristics of magnetite, *Chem. Geol.* 547 (2020) 119669, <https://doi.org/10.1016/j.chemgeo.2020.119669>.
- [22] A. Taufiq, A. Nikmah, A. Hidayat, S. Sunaryono, N. Mufti, N. Hidayat, H. Susanto, Synthesis of magnetite/silica nanocomposites from natural sand to create a drug delivery vehicle, *Heliyon* 6 (2020), e03784, <https://doi.org/10.1016/j.heliyon.2020.e03784>.
- [23] A. Taufiq, R.E. Saputro, D. Yuliantika, S. Sunaryono, M. Diantoro, A. Hidayat, N. Hidayat, M. Munasir, Synthesis of magnetite/silica nanocomposites from natural sand to create a drug delivery vehicle, *J. King Saud Univ. Sci.* 32 (2020) 3032–3038, <https://doi.org/10.1016/j.jksus.2020.08.009>.
- [24] E. Darezeshki, A.K. Dardan, M. Abdollahy, A.J. Zanjani, Synthesis of magnetite nanoparticles from iron ore tailings using a novel reduction-precipitation method, *J. Alloys Compd.* 749 (2018) 336–343, <https://doi.org/10.1016/j.jallcom.2018.03.278>.
- [25] V.A.R. Villages, J.I.D.L. Ramires, E.H. Guevara, S.P. Sicairos, L.A.H. Ayala, B. L. Sanchez, Synthesis and characterization of magnetite nanoparticles for photocatalysis of nitrobenzene, *Journal of Saudi Chemical Society* 24 (2020) 223–235, <https://doi.org/10.1016/j.jscs.2019.12.004>.
- [26] R. Rahmawati, M.G. Permana, B. Harison, Nugraha, B. Yulianto, D. Suyatman, Kurniadi, Optimization of frequency and stirring rate for synthesis of magnetite (Fe_3O_4) nanoparticles by using coprecipitation- ultrasonic irradiation methods, *Procedia Engineering* 170 (2017) 55–59, <https://doi.org/10.1016/j.proeng.2017.03.010>.
- [27] M.A.R. Beasley, E.J. Bartelink, L. Taylor, R.M. Miller, Comparison of transmission FTIR, ATR, and DRIFT spectra: implications for assessment of bone bioapatite diagenesis, *J. Archaeol. Sci.* 46 (2014) 16–22, <https://doi.org/10.1016/j.jas.2014.03.008>.
- [28] J.A.F. Garcia, A.I.D. Cano, A.G. Cervantes, J.S. Salazar, Magnetic domain interactions of Fe_3O_4 nanoparticles embedded in a SiO_2 matrix, *Sci. Rep.* 8 (2018) 5096, <https://doi.org/10.1038/s41598-018-23460-w>.
- [29] Gh.H. Khorrani, A. K. Zak, A. Kompany, R. Yousefi, Optical and structural properties of X-doped ($X = \text{Mn}, \text{Mg}, \text{and Zn}$) PZT nanoparticles by Kramers–Kronig and size strain plot methods, *Ceram. Int.* 38 (2012) 5683–5690, <https://doi.org/10.1016/j.ceramint.2012.04.012>.
- [30] S. Ilyas, Heryanto, B. Abdullah, D. Tahir, X-ray diffraction analysis of nanocomposite Fe_3O_4 /activated carbon by Williamson–Hall and size-strain plot methods, *Nano-Structures & Nano-Objects* 20 (2019) 100396, <https://doi.org/10.1016/j.nano.2019.100396>.
- [31] D. Tahir, S. Ilyas, B. Abdullah, B. Armynah, K. Kim, H.J. Kang, Modification in electronic, structural, and magnetic properties based on composition of composites Copper (II) Oxide (CuO) and carbonaceous material, *Mater. Res. Express* 6 (2019), 035705, <https://doi.org/10.1088/2053-1591/aafda>.
- [32] M. Holmboe, S. Wold, M. Jonsson, Porosity investigation of compacted bentonite using XRD profile modeling, *J. Contam. Hydrol.* 128 (2012) 19–32, <https://doi.org/10.1016/j.jconhyd.2011.10.005>.
- [33] B. Heryanto, D. Abdullah, Mahdalia Tahir, Quantitative analysis of X-ray diffraction spectra for determine structural properties and deformation energy of Al, Cu and Si, *J. Phys.: Conf. Ser.* 1317 (2019), 012052, <https://doi.org/10.1088/1742-6596/1317/1/012052>.
- [34] Hendri Heryanto, B. Abdullah, D. Tahir, Analysis of structural properties of X-ray diffraction for composite copper-activated carbon by modified Williamson Hall and size-strain plotting methods, *J. Phys.: Conf. Ser.* 1080 (2018), 012007, <https://doi.org/10.1088/1742-6596/1080/1/012007>.
- [35] S. Wu, A. Sun, F. Zhai, J. Wang, W. Xu, Q. Zhang, A.A. Volinsky, Fe_3O_4 magnetic nanoparticle synthesis from tailings by ultrasonic chemical co-precipitation, *J. Mater. Lett.* 65 (2011) 1882–1884, <https://doi.org/10.1016/j.matlet.2011.03.065>.
- [36] Heryanto, B. Abdullah, D. Tahir, Determination of binding energy for Cu and Cu_2O based X-ray diffraction spectrum, *J. Phys. Conf.* 979 (2018), 012055, <https://doi.org/10.1088/1742-6596/979/1/012055>.
- [37] D. Nath, F. Singh, R. Das, X-ray diffraction analysis by Williamson-Hall Halder wagner and size strain plot methods of CdSe nanoparticles-a comparative study, *Mater. Chem. Phys.* 239 (2020) 122021, <https://doi.org/10.1016/j.matchemphys.2019.122021>.
- [38] P. Scardi, M. Ermirich, A. Fitch, E.-W. Huang, R. Jardin, R. Kuzel, A. Leinewber, A. Mendoza Cuevas, S.T. Misture, L. Rebuffi, C. Schimpf, Size-strain separation in diffraction line profile analysis, *J. Appl. Crystallogr.* 51 (2018) 831–843, <https://doi.org/10.1107/S16005767180005411>.
- [39] D. Tahir, H. Heryanto, S. Ilyas, A.N. Fahri, R. Rahmat, M.H. Rahmi, Y. Taryana, S. G. Sukaryo, Excellent electromagnetic wave absorption of $\text{Co}/\text{Fe}_2\text{O}_3$ composites by additional activated carbon for tuning the optical and magnetic properties, *J. Alloys Compd.* 864 (2021) 158780, <https://doi.org/10.1016/j.jallcom.2021.158780>.
- [40] A. Taufiq, Sunaryono, E.G.R. Putra, A. Okazawa, I. Watanabe, N. Kojima, S. Pratapa, Darminto, nanoscale clustering and magnetic properties of $\text{Mn}_x\text{Fe}_{3-x}\text{O}_4$ particles prepared from natural magnetite, *Supercond. Nov. Magn.* 28 (2015) 2855–2863, <https://doi.org/10.1007/s10948-015-3111-9>.
- [41] A. Rayerfrancis, P.B. Bhargav, N. Ahmed, B. Chandra, S. Dhara, Effect of pH on the morphology of ZnO nanostructures and its influence on structural and optical properties, *Physica B* 457 (2015) 96–102, <https://doi.org/10.1016/j.physb.2014.09.044>.
- [42] B. Abdullah, S. Ilyas, D. Tahir, Nanocomposites $\text{Fe}/\text{activated carbon}/\text{PVA}$ for Microwave Absorber: synthesis and characterization, *J. Nanomater.* 2018 (2018), <https://doi.org/10.1155/2018/9823263>, ID 982326.
- [43] P.B. Khoza, M.J. Moloto, L.M. Sikhwhivulu, The effect of solvents, acetone, water, and ethanol, on the morphological and optical properties of ZnO nanoparticles prepared by microwave, *Journal of Nanotechnology* (2012) 195106, <https://doi.org/10.1155/2012/195106>.

- [44] R. Swanepoel, Determination of the thickness and optical constants of amorphous silicon, *J. Phys. E Sci. Instrum.* 16 (1983) 1214. <http://iopscience.iop.org/0022-3735/16/12/023>.
- [45] D.C. Look, J.H. Leach, On the accurate determination of absorption coefficient from reflectance and transmittance measurements: application to Fe-doped GaN, *J. Vac. Sci. Technol. B* 34 (2016) 04J105, <https://doi.org/10.1116/1.4954211>.
- [46] M. Ghasemifard, E. Fathi, M. Ghamari, The effect of Fe³⁺-doped on structure and optical properties of mesoporous Al₂O₃/SiO₂ composite, *Mater. Sci. Semicond. Process.* 42 (2016) 349–353, <https://doi.org/10.1016/j.mssp.2015.11.001>.
- [47] M.A. Mathrammel, A.M. Aboraia, M. Shkir, I.S. Yahia, M.A. Assiri, H.Y. Zahran, V. Ganesh, S. Alfaify, A.V. Soldatov, Optical analysis of nanostructured rose Bengal thin films using Kramers-Kronig approach: new trend in laser power attenuation, *Optic and Laser technology* 112 (2019) 207–214, <https://doi.org/10.1016/j.optlastec.2018.11.024>.
- [48] R.M. Al Mohaimeed, A.A. Ansari, A. Aldwayyan, The role of solvent environment on the optical behavior of chemically synthesized nanoparticles, *Journal of Spectroscopy* (2018) 6870645, <https://doi.org/10.1155/2018/6870645>.
- [49] D. Tahir, H.L. Kwon, H.C. Shin, S.K. Oh, H.J. Kang, S. Heo, J.G. Chung, J.C. Lee, S. Tougaard, Electronic and optical properties of Al₂O₃/SiO₂ thin films grown on Si substrate, *J. Phys. Appl. Phys.* 43 (2010) 255301, <https://doi.org/10.1088/0022-3727/43/25/255301>.
- [50] D. Tahir, S.K. Oh, H.J. Kang, S. Tougaard, Composition dependence of dielectric and optical properties of Hf-Zr-silicate thin films grown on Si (100) by atomic layer deposition, *Thin Solid Films* 616 (2016) 425–430, <https://doi.org/10.1016/j.tsf.2016.09.001>.
- [51] D. Tahir, S. Tougaard, Electronic and optical properties of selected polymers studied by reflection electron energy loss spectroscopy, *J. Appl. Phys.* 111 (2012), 054101, <https://doi.org/10.1063/1.3688327>.
- [52] D. Tahir, S.K. Oh, H.J. Kang, S. Tougaard, Quantitative analysis of reflection electron energy loss spectra to determine electronic and optical properties of Fe-Ni alloy thin films, *J. Electron. Spectrosc. Relat. Phenom.* 206 (2016) 6–11, <https://doi.org/10.1016/j.elspec.2015.11.005>.
- [53] D. Tahir, Suarga, N.H. Sari, Yulianti, Stopping powers and in elastic mean free path of 200eV–50 keV electrons in polymer PMMA, PE, and PVC, *Appl. Radiat. Isot.* 95 (2015) 59–62.
- [54] S. Suryani, Heryanto, D. Tahir, Stopping powers and inelastic mean free path from quantitative analysis of experimental REELS spectra for electrons in Ti, Fe, Ni, and Pd, *Surf. Interface Anal.* 52 (2019) 16–22, <https://doi.org/10.1002/sia.6713>.
- [55] S. Suryani, Rusdaeni Heryanto, A.N. Fahri, D. Tahir, Quantitative analysis of diffraction and infra-red spectra of composite cement/BaSO₄/Fe₃O₄ for determining correlation between attenuation coefficient, structural and optical properties, *Ceram. Int.* 46 (11) (2020) 18601–18607, <https://doi.org/10.1016/j.ceramint.2020.04.170>.
- [56] Heryanto Nurhasmi, A.N. Fahri, S. Ilyas, A. Ansar, B. Abdullah, D. Tahir, Study on optical phonon vibration and gamma ray shielding properties of composite geopolymer fly ash-metal, *Radiat. Phys. Chem.* 180 (2021) 109250, <https://doi.org/10.1016/j.radphyschem.2020.109250>.
- [57] Y. Kirana, H. Heryanto, S. Ilyas, A.N. Fahri, B. Abdullah, D. Tahir, Optical properties determined from infrared spectroscopy and structural properties from diffraction spectroscopy of composites Fe/CNs/PVA for electromagnetic wave absorption, *Opt. Mater.* 111 (2021) 110639, <https://doi.org/10.1016/j.optmat.2020.110639>.
- [58] O.S. Jangong, H. Heryanto, R. Rahmat, I. Mutmainna, P.L. Gareso, D. Tahir, Effect of sugar palm fiber (SPF) to the structural and optical properties of bioplastic (SPF/Starch/Chitosan/Polypropylene) in supporting mechanical properties and degradation performance, *J. Polym. Environ.* (2021), <https://doi.org/10.1007/s10924-020-02019-9>.
- [59] N. Rauf, S. Ilyas, H. Heryanto, R. Rahmat, A.N. Fahri, M.H. Rahmi, D. Tahir, The correlation between structural and optical properties of zinc hydroxide nanoparticle in supports photocatalytic performance, *Opt. Mater.* 112 (2021) 110780, <https://doi.org/10.1016/j.optmat.2020.110780>.
- [60] L.H. Omari, H. Lemziouka, R. Moubah, M. Haddad, H. Lassri, Structural and optical properties of Fe-doped ruddlesden-popper Ca₃Ti_{2-x}Fe_xO_{7-δ} nanoparticles, *Mater. Chem. Phys.* 246 (2020) 122810, <https://doi.org/10.1016/j.matchemphys.2020.122810>.
- [61] Y.V. Vorobiev, P.P. Horley, J.H. Borja, H.E. Ponce, R.R. Bon, P. Vorobiev, C. Pérez, J.G. Hernández, The effects of porosity on optical properties of semiconductor chalcogenide films obtained by the chemical bath deposition, *Nanoscale Research Letters* 7 (2012) 483, <https://doi.org/10.1186/1556-276X-7-483>.